12-1-2004

Laboratory Experiments of Entrainment in Dry Convective Boundary Layers

Harm J.J. Jonker
Delft University of Technology, h.jonker@ws.tn.tudelft.nl

Thijs Heus
Delft University of Technology, t.heus@csuohio.edu

Esther Hagen
Delft University of Technology

Han Van Dop
Utrecht University

4.25 LABORATORY EXPERIMENTS OF ENTRAINMENT IN DRY CONVECTIVE BOUNDARY LAYERS

Harm J.J. Jonker*, Thijs Heus, Esther Hagen,
Thermal and Fluids Sciences Section, Delft University of Technology, The Netherlands
and Han van Dop, IMAU, Utrecht University, The Netherlands

1. INTRODUCTION

The entrainment flux across the inversion is still an important issue in convective atmospheric boundary layers; see for a recent discussion Fedorovich et al. (2004). For the dry convective boundary layer, *communis opinio* seems to have it that the entrainment buoyancy flux can be readily expressed in terms of the surface buoyancy flux by:

$$\overline{w'b'}_e = -A\,\overline{w'b'}_0 \tag{1}$$

where the factor A incorporates a mild dependence on the Richardson number Ri (as a measure of the relative inversion strength) to account for the depth of the entrainment zone (e.g. Sullivan et al., 1998; vanZanten et al., 1998; Lewellen and Lewellen, 1998). For large values of Ri (small entrainment zones), A is thought to reach a saturation value between 0.1 and 0.2 - a view corroborated by large eddy simulations (e.g. Fedorovich et al., 2004). Within the framework of a zero-order model, equation (1) is equivalent to stating that the non-dimensional entrainment rate is inversely proportional to the Richardson number, i.e.

$$\frac{w_e}{w_*} = A\mathrm{Ri}^{-1} \tag{2}$$

where $w_e = dz_i/dt$ denotes the entrainment velocity, $w_* = (z_i\,\overline{w'b'}_0)^{1/3}$ represents the convective velocity scale, and where Ri denotes the Richardson number based on the buoyancy jump Δb across the inversion

$$\mathrm{Ri} = \frac{\Delta b\, z_i}{w_*^2} \tag{3}$$

A generalized version of (2) is $w_e/w_* \sim \mathrm{Ri}^{\alpha}$; for a comprehensive discussion on the "entrainment exponent" α in relation to varying experimental settings (oscillating grids, surface stress, impingement, etc.), as well as to Reynolds, Schmidt and Prandtl-number effects, see Cotel and Breidenthal (1997). Laboratory experiments on entrainment with a thermally driven convection tank, carried out by Deardorff et al. (1980), were not conclusive to choose whether a Ri^{-1}-law, or a $\mathrm{Ri}^{-3/2}$-law (Turner, 1973) would be more appropriate, although the authors were inclined to favour the Ri^{-1}-law based on their data.

In this study we show preliminary experimental evidence that cast some doubts on the validity of (1) (and therefore also on (2)) in the range of large Richardson numbers.

*Corresponding author address: Harm J.J. Jonker, Thermal and Fluids Sciences, Dept. of Multi-Scale Physics, Delft University of Technology, Lorentzweg 1, 2628CJ Delft, The Netherlands, e-mail: h.jonker@ws.tn.tudelft.nl

We make use of a saline convection tank set-up as a laboratory model for a dry convective atmospheric boundary layer (e.g. Hibberd and Sawford, 1994). Its lateral dimensions are 1m x 1m, and the typical boundary layer depth ranges is 0.1m. Rather than starting with a salinity lapse-rate, we begin with a two-layer system, where on top of the saline layer (the mixed layer) we have carefully placed a layer with lower salinity concentration, thus creating a well-defined inversion jump. In contrast to previous studies on entrainment, we do not so much focus on the entrainment velocity w_e, but rather on the entrainment flux, which we measure with Planar Laser Induced Fluorescence (PLIF). Several experiments have been carried out over a wide range of inversion strengths (Ri ranging from 18 to 146). From the resulting PLIF-sheets vertical flux profiles have been derived. The most striking observation is that the entrainment flux is found to reveal a much stronger dependence on the inversion strength (Ri) than large eddy simulations tend to do: especially for large Richardson numbers, the entrainment flux is found to vanish, rather than to converge to a constant non-zero value.

2. EXPERIMENTAL SET-UP AND MEASUREMENT METHODS

The saline convection tank set-up that was used in this study is sketched in Fig. 1. It consists of a glass container with an inner size of 1x1x0.6m; in it resides a perspex tray with an outer size of 98x98x10cm. The inner tray is filled with fresh water. On top of the tray resides the mixed layer with a salinity concentration of S_1. Because the mixed layer fluid has a higher density than the water in the lower tray, a filter cloth between two perforated metal plates was attached to prevent autonomous mixing of the two layers. A homogeneous surface buoyancy flux was created by connecting the lower tray to an elevated 300l sized storage tank which fills the tray during the experiment and consequently forces fresh water through the permeable filter with a velocity in the order of $w_d \sim 10^{-5}$m/s. The resulting surface buoyancy flux depends on w_d and the density difference $\Delta\rho$ through:

$$B_0 = g w_d \frac{\Delta\rho}{\rho_1} \tag{4}$$

where ρ_1 denotes the mixed layer density. We used a relative density difference of 0.5%, which, together with $w_d = 5 \cdot 10^{-5}$m/s, leads to $B_0 = 2.5 \cdot 10^{-5}\mathrm{m}^2/\mathrm{s}^3$.

Rather than starting with a salinity lapse-rate, we initiate the experiments with a two-layer system: on top of

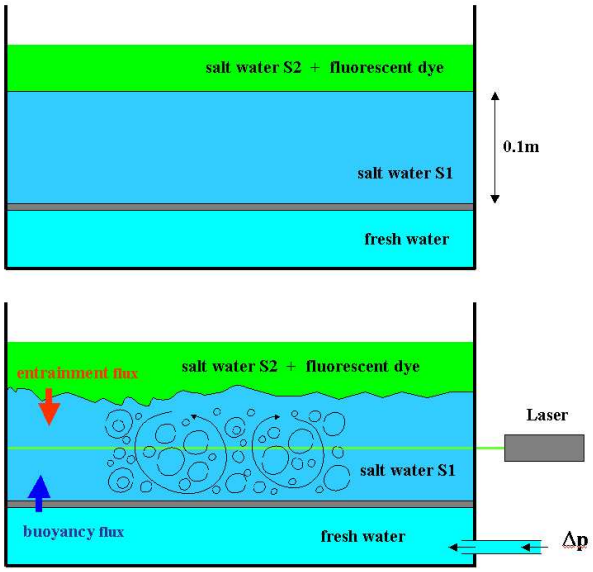

FIG. 1: Sketch of the used set-up. Top: initial (stable) two-layer system. The salt concentration of the mixed layer S_1 is larger than the top layer S_2, creating a stable situation with a well defined density difference $\Delta\rho = \rho_1 - \rho_2$. A rigid filter keeps the water in the mixed layer and the lower tray separated. Bottom: by externally filling the lower tray, less dense water is forced through the filter into the mixed layer, creating a surface buoyancy flux.

the mixed layer we carefully placed a layer with lower salinity concentration, thus creating a well-defined (inversion) density jump: $\Delta\rho = \rho_2 - \rho_1$. this density jump was varied between the experiments. There was no lapse rate above the inversion. The initial mixed layer height was $z_i = 0.1$m in all experiments. Using these numbers we arrive at a convective velocity scale of

$$w_* = (B_0 z_i)^{1/3} = 1.3 \cdot 10^{-2}\text{m/s}$$

Note that $w_*/w_d \gg 1$. The Reynolds number based on w_* and z_i is Re ≈ 1350; the Peclet number is Pe $=$ ReSc $= \mathcal{O}(10^6)$, because of the large Schmidt number Sc $\sim 10^3$. The strength of the inversion relative to the convective process is indicated by the Richardson number (similar to (3))

$$\text{Ri} = \frac{g z_i \Delta\rho}{w_*^2 \rho_1} \qquad (5)$$

Several experiments have been carried out over a wide range of inversion strengths: while the value of w_* was kept (approximately) constant between the experiments, the Richardson number ranged between 18 and 146. The turbulence velocities have been measured using Particle Image Velocimetry (PIV), in order to test whether the convection tank set-up displayed the correct CBL characteristics (which was found satisfactory).

The entrainment flux was measured using Planar Laser Induced Fluorescence (PLIF). By adding a fluorescent dye (dissodium fluorescein) to the inversion layer (top layer in Fig. 1), one can directly visualize the mass entrained from the inversion layer into the mixed layer (see Figs. 2-6). To this end a vertical laser sheet was created using rotating polygonal mirror, while the intensity of fluorescence in the x, z-plane was captured with a digital camera. The resulting images were corrected for laser attenuation owing to the absorption by the dye, after which the dye concentration $c(x, z, t)$ could be derived. From the average profiles $\overline{c}(z, t)$, it is possible to determine concentration fluxes by inverting the relation

$$\frac{\partial \overline{c}}{\partial t} = -\frac{\partial \overline{w'c'}}{\partial z} \quad \rightarrow \quad \overline{w'c'}(z,t) = -\int \frac{\partial \overline{c}(z',t)}{\partial t} dz' \qquad (6)$$

It should be emphasized that this method measures the dye entrainment flux, rather than the buoyancy entrainment flux. However, these fluxes are of course related. For example, within the zero-order framework,

$$\overline{w'c'}_e = -w_e \Delta C = \overline{w'b'}_e \frac{\Delta C}{\Delta b}$$

Since ΔC and Δb are both non-zero and finite, a vanishing dye entrainment flux implies a vanishing buoyancy entrainment flux.

3. RESULTS

In figures 2-6 the corrected PLIF images are displayed. The resulting concentration profiles are displayed in Figs. 7-8 for increasing Ri. Visual inspection of the "raw" images Fig. 2-6, show the striking difference between low and high Richardson numbers. For low values of Ri, one observes the typical downdraft structures which transport the entrained dye into the mixed layer, after which mixing takes place. For larger Richardson numbers, (Ri ≥ 82), the convection (i.e. impinging plumes) does not seem capable anymore of breaking or disrupting the density interface. Although an animation of the images clearly reveals waves traveling along the interface, initiated by the impinging plumes, the interface does not loose its integrity. Put differently, relative to the strength of the inversion, the convection appears to be too weak to generate entrainment. The concentration profiles, displayed in Figs. 7-8 show the same effect. For low Ri one can observe a steady increase of the dye concentration in the mixed layer, as well as an increase of the mixed layer height in time (Fig. 7). For high Ri, however, there is hardly any increase of dye in the mixed layer; the small increase of the inversion height results from the surface mass-flow rate w_d.

Although preliminary, these results cast some doubts on the validity of the "constant" entrainment relation (1) for situations with large Richardson numbers, and, perhaps of relevance, in absence of a lapse-rate aloft. More experiments are currently being carried out with an improved set-up.

REFERENCES

Cotel, A. and R. Breidenthal, 1997: A model of stratified entrainment using vortex persistence. *Appl. Sci. Res.*, **57**, 349–366.

Deardorff, J., G. Willis, and B. Stockton, 1980: Laboratory studies of the entrainment zone of a convectively mixed layer. *J. Fluid Mech.*, **100**, 41–64.

Fedorovich, E., R. Conzemius, and D. Mironov, 2004: Convective entrainment into a shear-free, linearly stratified atmosphere: bulk models reevaluated through large-eddy simulations. *J. Atmos. Sci.*, **61**, 281–295.

Hibberd, M. and B. Sawford, 1994: Design criteria for water tank models of dispersion in the planetary convective boundary layer. *Bound.-Layer Meteor.*, **67**(97-118).

Lewellen, D. and W. Lewellen, 1998: Large eddy boundary layer entrainment. *J. Atmos. Sciences*, **55**, 2645–2665.

Sullivan, P., C.-H. Moeng, B. Stevens, D. Lenschow, and S. Mayor, 1998: Structure of the entrainment zone capping he convective atmospheric boundary layer. *J. Atmos. Sci.*, **55**, 3042–3064.

Turner, J., 1973: *Buoyancy effects in fluids*. Cambridge University Press.

vanZanten, M. C., P. G. Duynkerke, and J. W. M. Cuijpers, 1998: Entrainment parameterization in convective boundary layers derived from large eddy simulations. *J. Atmos. Sci.*, **56**, 813–828.

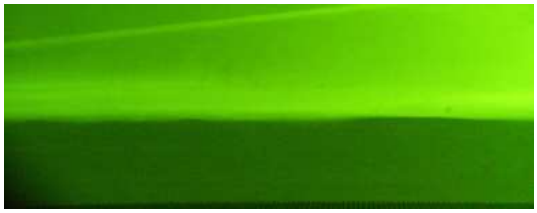

(a) $t = 2t_*$

(b) $t = 4t_*$

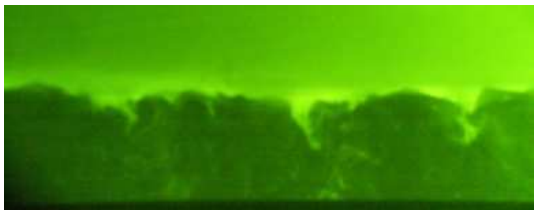

(c) $t = 6t_*$

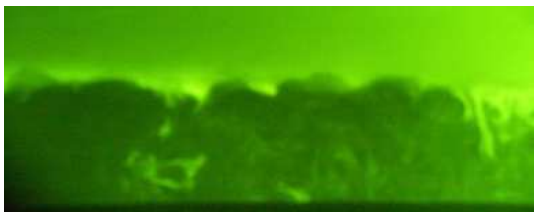

(d) $t = 8t_*$

FIG. 2: Ri $= 18$.

(a) $t = 2t_*$

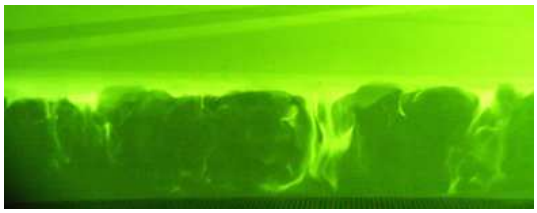

(b) $t = 4t_*$

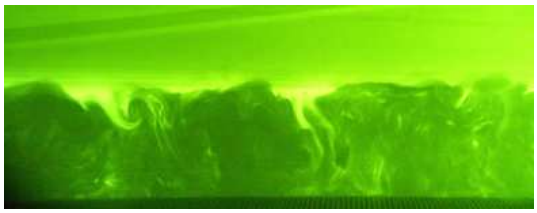

(c) $t = 6t_*$

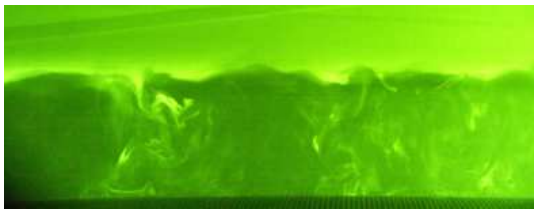

(d) $t = 8t_*$

FIG. 3: Ri $= 37$.

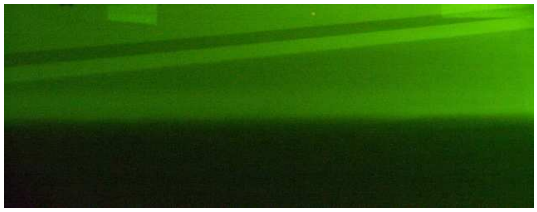

(a) $t = 2t_*$

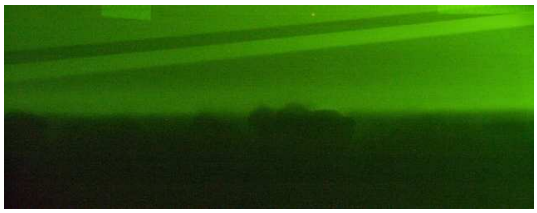

(b) $t = 4t_*$

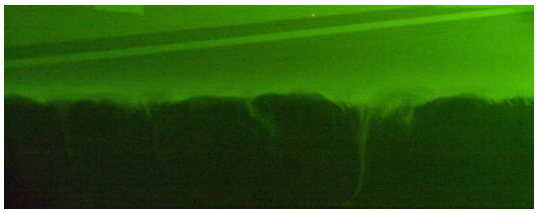

(c) $t = 6t_*$

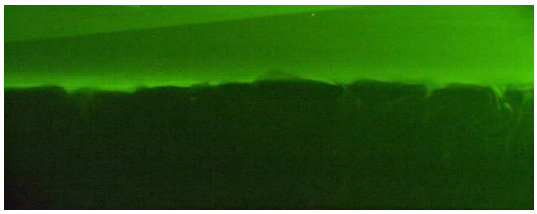

(d) $t = 8t_*$

FIG. 4: Ri $= 42$.

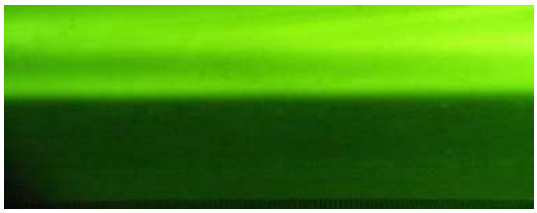

(a) $t = 2t_*$

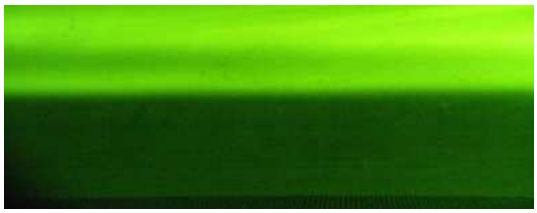

(b) $t = 4t_*$

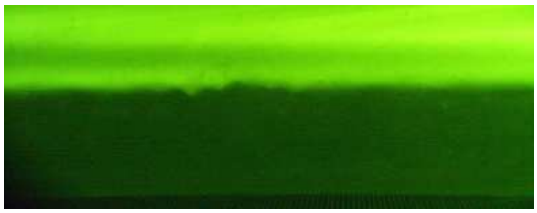

(c) $t = 6t_*$

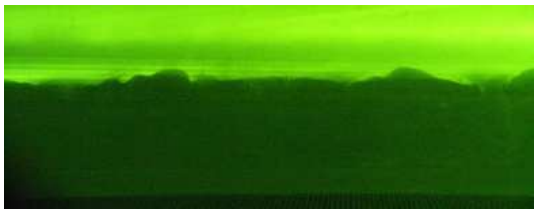

(d) $t = 8t_*$

FIG. 5: Ri $= 82$.

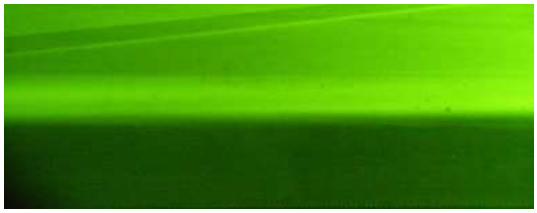

(a) $t = 2t_*$

(b) $t = 4t_*$

(c) $t = 6t_*$

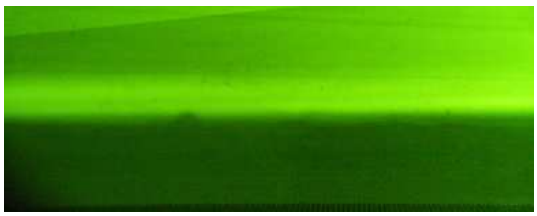

(d) $t = 8t_*$

FIG. 6: Ri $= 146$.

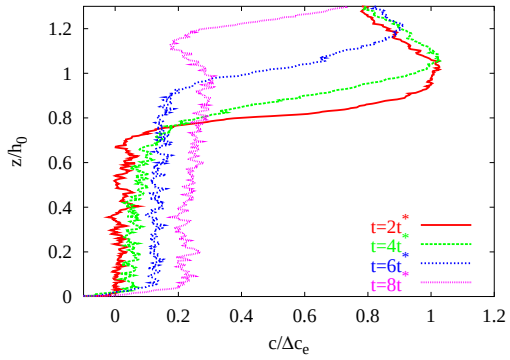

(a) Ri $= 18$

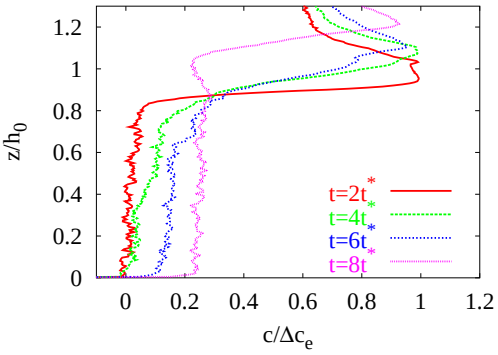

(b) Ri $= 37$

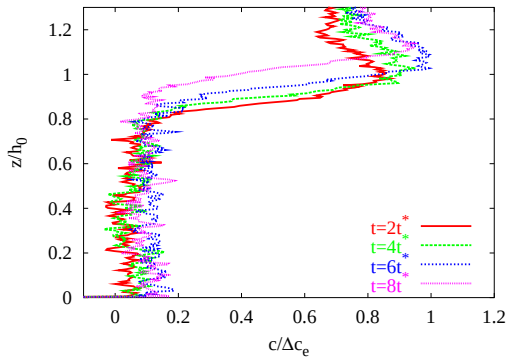

(c) Ri $= 42$

FIG. 7: Dye concentration profiles derived from the experiments.

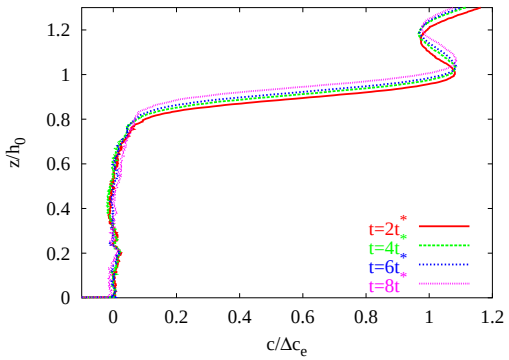

(a) Ri $= 82$

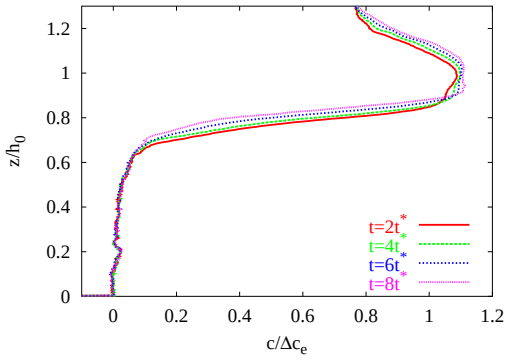

(b) Ri $= 146$

FIG. 8: Dye concentration profiles derived from the experiments.